



Polymer electrolyte membranes with exceptional conductivity anisotropy via holographic polymerization

Derrick M. Smith ^a, Shan Cheng ^a, Wenda Wang ^a, Timothy J. Bunning ^b, Christopher Y. Li ^{a,*}

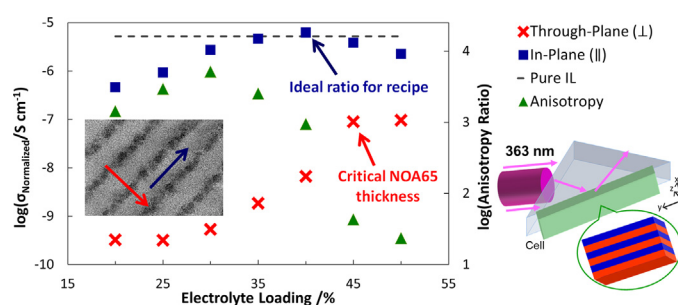
^a Department of Material Science and Engineering, Drexel University, 3141 Chestnut Street, Philadelphia, 19104 PA, USA

^b Air Force Research Laboratory, Materials & Manufacturing Directorate, Wright-Patterson AFB, OH 45433, USA

HIGHLIGHTS

- Holographic polymer electrolyte membranes have been fabricated.
- They are comprised of alternating nanolayers of ionic liquids and crosslinked resin.
- The membrane has an ionic conductivity anisotropy of ~5000.

GRAPHICAL ABSTRACT



ARTICLE INFO

Article history:

Received 15 April 2014

Received in revised form

26 July 2014

Accepted 26 July 2014

Available online 14 August 2014

Keywords:

Polymer electrolyte membrane
Solid polymer electrolytes
Ion conducting
Holographic polymerization
Photopolymerization
Ionic liquid

ABSTRACT

Polymer electrolyte membranes using an ionic liquid as electrolyte with an ionic conductivity anisotropy of ~5000 have been fabricated using a holographic polymerization nanomanufacturing technique. The resultant structure is referred to as holographic polymer electrolyte membranes (hPEMs), which are comprised of alternating nanolayers of a room temperature ionic liquid and crosslinked polymer resin, confirmed under TEM imaging. These hPEMs also show no reduction in room temperature conductivity with respect to the loaded ionic liquid when characterized in the plane of ionic liquid nanolayers. At elevated temperatures with the optimal electrolyte volume loading, calculation shows that the free ion concentration is higher than the pure ionic liquid, suggesting that the photopolymer dual-functionalizes as a loadbearing scaffold and an ion-complexing agent, allowing for more ions to participate in charge transfer. These hPEMs provide a promising solution to decoupling mechanical enhancement and ion transport in polymer electrolyte membranes.

© 2014 Elsevier B.V. All rights reserved.

1. Introduction

Polymer films with directional preference for ion transport are desirable for electrochemical, [1,2] purification, [3,4] sensor and stimuli-response, [5] and organic transistor [6] applications as the anisotropy can increase mass transport efficiency, permeability,

sensitivity and response times, and reduce gate leakage in the non-preferred direction. Anisotropic ion conducting films were first reported in 1995 in Nafion films after melt processing, where an anisotropy of 1.4 was reported. [7] Since then, applying external mechanical, [7–10] electrical [10] or magnetic fields, [11,12] solvent casting methods, [13] electrospraying block-co-polymers (BCPs), [14] liquid crystals polymer templating, [9,15–17] and tailoring crystalline polymer morphology have been demonstrated to increase ion flux anisotropy in polymer electrolyte films; however, there remains

* Corresponding author.

E-mail address: chrisli@drexel.edu (C.Y. Li).

hurdles for each of these techniques to effectively direct ion transport, both from processing and device standpoints. Conductivity anisotropies of up to 10–12 can be achieved with single-step solution casting, [13] and higher anisotropies can be demonstrated via secondary processing techniques: 20 for mechanical stretching, [18] 75 for melt pressing diblock-copolymers, [10] and approaching 1000 for liquid crystalline BCPs aligned under an external 6 T magnetic field. [11] Of particular interest for this work is anisotropic conducting behavior in solid polymer electrolyte membranes (PEMs) for fuel cell and battery applications. PEMs with high conductivity and high mechanical integrity are critical for energy related applications including solid state batteries and fuel cells. For PEMs, since ion transportation is enabled by segmental motion of the host polymer matrix, modifying the membranes for enhanced mechanical properties often has a direct negative effect on the ionic transport properties. To address this structural/property tradeoff, films with highly ordered directionalized transport nanostructures have been employed to incorporate rigid load-bearing scaffolds which minimize any detrimental effects to the through-plane ionic conductivity. BCP PEMs with two distinct ion-conducting and load-bearing phases have shown great promise in addressing this property tradeoff. However, incorporating long-range order in these anisotropic films is difficult, as BCP grain boundaries typically introduce ion tortuosity. Correlation between BCP phase morphology and ionic conductivity is still a subject of intense study [19–21]. We report a new Holographic Polymerization (HP) system using Norland Optical Adhesive 65 (NOA65) as the photopolymerizable cross-linking resin, and an ionic liquid (IL) as the electrolyte, BrTHTDP, to convert a liquid electrolyte to a bulk solid free-standing film, decoupling mechanical enhancement and ion transport properties, resulting in films with anisotropic conductivity of ~5000.

HP is a relatively simple and effective top-down technique to fabricate ordered nanostructures [22]. A photopolymerizable syrup, typically consisting of monomers, photoinitiator, and often inert materials, is exposed to two or more coherent laser beams whose interference creates a periodic standing wave pattern on a length scale dictated by the interference angle and the laser source. This results in spatially periodic polymer-rich and polymer-poor domain structures whose local morphology is driven by the complex interplay of reaction, phase separation, and transport dynamics. Simplistically, the photopolymerizable resin component diffuses into and reacts in the constructive interference volumes, and the non-reactive species is driven or transported into the local areas of destructive (dark) interference volumes. Typically a multifunctional monomer is polymerized via chain or step growth polymerization, enabled by a photoinitiator and coinitiator, combined with a reactive diluent to control polymerized network growth, and a non-reactive species. Materials that have been periodically patterned via HP include liquid crystals [22,23], nanoparticles, [24–27] homopolymers, [28,29] and BCPs [30,31]. Most recently, we showed that using polyethylene oxide (PEO) and a bis(trifluoromethane)sulfonimide lithium salt (LiTFSI) electrolyte as the photo-inert material, fabrication of anisotropic PEMs for batteries could be obtained. [32] However, because a brick-and-mortar semi-continuous morphology was formed instead of continuous layers; an in-plane/through-plane conductivity ratio of approximately 35 was achieved. While already a 3-fold improvement over one-step thin film synthesis techniques, much available improvement exists by optimizing the morphology.

2. Experimental section

2.1. Materials

Trihexyltetradecylphosphonium bromide (BrTHTDP) ionic liquid (IL) was purchased from Aldrich; the crosslinkable monomer

system Norland Optical Adhesive 65 (NOA-65) was purchased from Norland Inc. A UV initiator, Darocure 4265 was graciously provided by CIBA-GEIGY Company. NOA-65 is proprietary information of Norland Products Inc, but is widely known to contain a tetrafunctional ene and a trifunctional thiol. The tetrafunctional ene in NOA-65 may contain two urethane groups per molecule.

2.2. Holographic polymerization

The output from a Coherent Ar-ion laser (model Sabre Innova 10R/2) with a laser wavelength of 363.8 nm and an output power of 240–270 mW was used for HP. The typical HP exposure time was 60 s. During the exposure, the laser beam enters the sample cell then reflects off of the glass/air surface of the sample wall and passes back through the cell (Fig. 1 shows the path of the laser beam). The overlap of the incoming and reflected beams result in a 1D interference pattern with the periodic intensity profile normal to the glass of the sample cell. In order to control the period of the grating, the prism and the cell assembly were placed on a rotation stage.

BrTHTDP, NOA65, Darocure 4265 and <0.01 w/w% 23 μm glass bead spacers were mixed in a vortex for 5 min, followed by sandwiching between two glass slides; the spacers were included to control the thickness of the membrane. The glass sandwich cell containing the prepolymer syrup was placed on the hypotenuse of an isosceles 90° glass prism as shown in Fig. 1, adhered with a Cargille refractive index fluid, with $n = 1.4900$ to match the prism for optical contact, via capillary force. The targeted PEMs have a lamellar structure with the lamellae parallel to the membrane

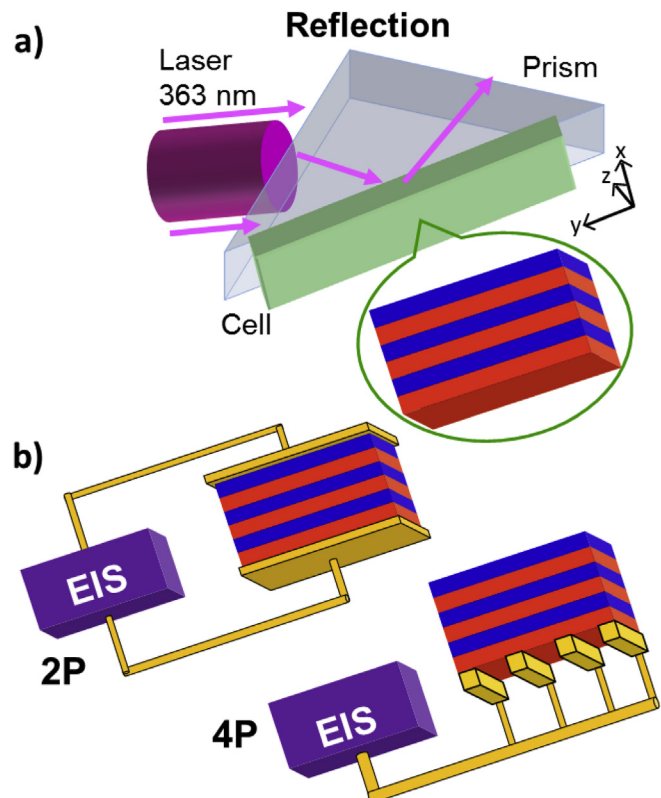


Fig. 1. (a) Schematic of optic setup for reflection hPEMs. (b) Schematic of the electrode configurations used to characterize the films' conductivity using a 4-line probe setup for in-plane conductivity (top) and a 2-point sandwich probe for through-plane conductivity (bottom). The blue and red layers represent NOA65-rich and IL-rich areas, respectively. (For interpretation of the references to color in this figure legend, the reader is referred to the web version of this article.)

surface (Fig. 1). Pre-polymer syrups are exposed to a reflection interference pattern for 60 s created by a 363.8 nm monochromatic, coherent light source provided by an Ion Coherent 308C laser. The glass sandwiches were then lifted from the prism for either optical cleaning with ethanol and acetone, or pried open for film extraction. Membranes were also polymerized without the interference pattern for comparison of the structural effect; membranes floodlit like this are denoted as isotropic PEMs (iPEMs).

2.3. Morphology characterization

UV–Vis was carried out with the glass sandwiches using an Ocean Optics fiber spectrometer, with light source and detector offset 0° from the normal to the plane of the film. The 100% transmission was normalized using a baseline from one microscope slide. Bright field TEM experiments were conducted using a JEOL JEM2100 with an accelerating voltage of 200 kV. TEM samples were prepared by removing the holograms from the glass sandwiches, followed by embedding in an Epoxy two part epoxy for 3 days. Hardened samples were microtomed into 80 nm sections using a Leica UC6 ultramicrotome with a Diatome diamond knife. Sections of the embedded reflection grating were floated on water and collected on Nickel grids. All the samples were stained with RuO₄ vapor for 45 min to enhance contrast. For TEMT, one drop of 10 nm Au nanoparticle aqueous solution was deposited on each side of the grid for 30 s to provide fiduciary markers for 3D reconstruction. The grid was rotated ±60° to the beam's normal along one axis with high resolution images collected at 1° increments.

2.4. Ion transport characterization

All samples were extracted from the glass sandwiches as free-standing films and vacuum dried at room temperature for 2 weeks, followed by aging in an Ar filled glove box for four weeks to assure proper post-curing, and that the films were dry. Two EIS setups are used to characterize PEMs both in-plane (||) and through-plane (⊥) to the lamellae employed using a Princeton Applied Research Parstat 2273 Potentiostat in conjunction with Powersuite® software, depicted in Fig. 1. A custom-made cell was constructed, where 2 sets of electrode PTFE molded slips with either 2 stainless steel electrode paddles, or 4 platinum wires and a PTFE substrate would sandwich the membrane sample. A third liquid cell setup was used for the IL and NOA65 monomer samples. An AC frequency was used in the range of 0.1 Hz–100 kHz and the resistance data was taken from the Nyquist plot. The extrapolated x-intercept value of the Nyquist plot's semi-circle regression is used as the resistance value, R , and plugged into the Eq. $\sigma = L/R * A$, where L is the electrode spacing and A is the cross-sectional area of the sample, to calculate the ionic conductivity. The cell was placed on an Instec hot stage for the temperature scans ranging from 35 °C to 115 °C in 10 °C steps; the samples were annealed at each temperature for 15 min before testing. Anisotropic conductivity is used to describe the ratio between the ionic conductivity in-plane to both the nanostructured lamellae and film, since their planes are parallel, versus the through-plane, or in the direction of the films' normal.

3. Results

ILs typically refer to salts with a melting temperature below 20–30 °C, [33] which exhibit electrolytic properties, a wide range of viscosities, and effectively have no vapor pressure. These unique characteristics position ILs to be a versatile green alternative for many temperature-sensitive applications involving mass, heat or charge transfer. BrHTDP was selected to facilitate the phase separation during the HP process. The nanomorphology formed in the

present system is attributed to the synergistic phase separation and photopolymerization processes which led to a ~5000 fold difference in ionic conductivity for in-plane and through-plane directions.

3.1. UV–Vis characterization

Fig. 2 shows UV–Vis spectra for the hPEMs reflection gratings. The y axes of the spectra are offset for clarity, with the diffraction efficiency (DE) magnitudes listed for each curve. All the spectra from the different electrolyte loadings show a near 100% background transmission in the visible region, with a sharp diffraction peak around 600 nm. For a typical reflection structure, droplet formation in lieu of lamellae causes a roll-off in the spectra near the UV region, and poor phase separation between the HP layers and electrolyte layers leads to broadening of the diffraction notches. The depth of the diffraction peaks is defined as the DE, and directly proportional to the refractive index mismatch between the two materials, which is also directly proportional to the HP partitioning efficiency, or the concentration profiles of each NOA65 and IL with respect to the normal of the lamellae nanostructure. At moderate electrolyte loadings around 30–35 w/w%, the DE is highest, suggesting the partitioning efficiency is maximized around these electrolyte loadings. The DE begins to slightly taper off as the electrolyte loading is increased or decreased; however, for all samples within the tested 15–50 w/w% electrolyte loading, the DEs were around 30–40% with 100% background transmissions, suggesting that consistently well-defined layers are formed regardless of electrolyte loading.

3.2. TEM and TEMT morphology characterization

To confirm the structure, transmission electron microscopy (TEM) and TEM tomography (TEMT) were performed on ~80 nm thick cross-sections of the films. Fig. 3 shows TEM images of various electrolyte loadings, where the dark domains are IL-rich regions and the lighter domains are cross-linked NOA65. Phase separated,

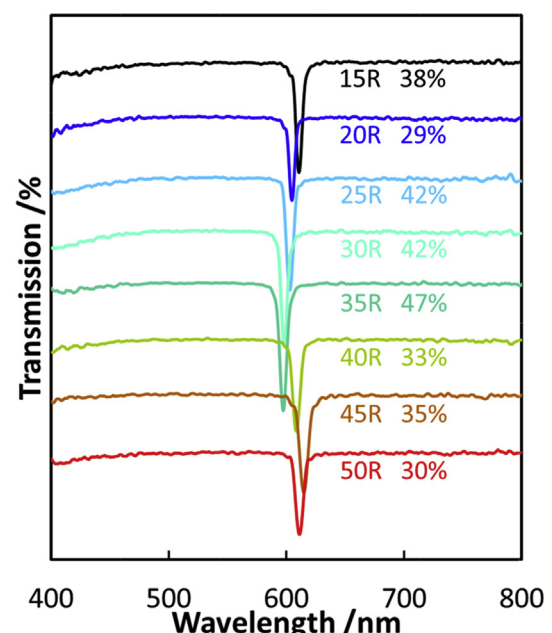


Fig. 2. UV–Vis spectra of hPEMs taken with source normal to the plane of the membranes for samples with 15–50 w/w% with corresponding first order Bragg diffraction efficiencies noted.

defect free, long-range continuous layers for both the IL and NOA65 can be seen clearly in all the samples. “Cross talk” of adjacent layers was not observed for either domain in any film characterized.

TEM shows the phase boundaries between the BrTHTDP and NOA65 for the 20% sample (Fig. 3a, b) are relatively clean with some fine interface texturing on the tens of nm scale; this behavior is consistent as the electrolyte volume is increased, with some degree of interface roughening at higher electrolyte loadings. As expected, as the IL loading is increased, the thickness of the stained regions increased. A general qualitative trend for the BrTHTDP is apparent

in that at higher IL loadings, the corresponding dark regions in TEM comprise more area of the micrograph. Throughout the range of volumes investigated, long-range continuous layers for both the BrTHTDP and NOA65 were observed. To further probe the morphology, TEMT was performed on select samples; an image of TEMT reconstruction can be seen Fig. 3i, and an isolated nanochannel in Fig. 3j, showing that the morphology of the nanochannels is relatively clean and consistent throughout the volume of the holograms. Videos of the TEMT reconstruction can be viewed in the Supporting information.

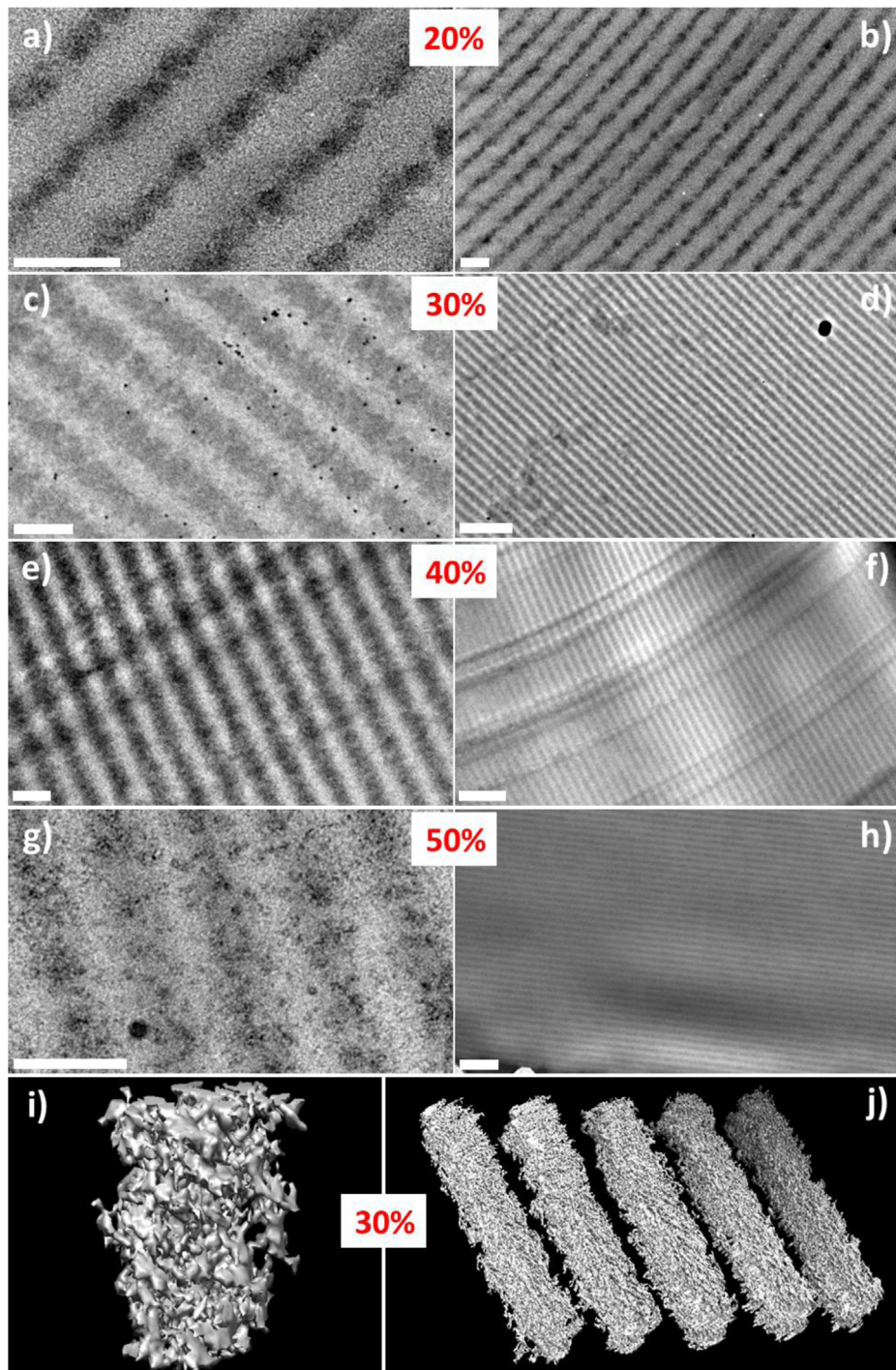


Fig. 3. TEM images of hPEMs. (a), (c), (e), and (g) Micrographs of 20–50 w/w% electrolyte with a scale bar of 200 nm. (b), (d), (f), and (h) Micrographs with a scale bar of 1 μ m. All samples were ultra-micromilled stained with RuO₄. 10 nm Au nanoparticle fiducial markers used for TEMT can be seen in the 30% sample. (i) and (j) TEMT reconstruction for 30 w/w%.

Supplementary video related to this article can be found at <http://dx.doi.org/10.1016/j.jpowsour.2014.07.172>.

3.3. Ionic conductivity using electrochemical impedance spectroscopy

For comparison, the pure IL and NOA65 monomer were tested and their ionic conductivities were measured as $5.28 \cdot 10^{-6} \text{ S cm}^{-1}$ and $3.59 \cdot 10^{-7} \text{ S cm}^{-1}$, respectively at room temperature. A film of just NOA65 was also photopolymerized, but the ionic conductivity was less than $6 \cdot 10^{-13} \text{ S cm}^{-1}$, which is the limit of our equipment. EIS was performed on the hPEMs to examine the effect of light directed phase separation on IL ion transport. Furthermore, normalized room temperature conductivity with respect to IL loading was calculated with Eq. (1):

$$\sigma_{\text{Normalized}} = \frac{\sigma}{v/v\% \text{Ionic Liquid}}; \quad (1)$$

normalized conductivities for \perp (σ_{\perp}) and (σ_{\parallel}) and resulting ionic conductivity anisotropy versus electrolyte loading is shown in Fig. 4. σ_{\parallel} varies moderately with increasing IL concentration and a maximum normalized conductivity is seen at 40 w/w% with $6.24 \cdot 10^{-6} \text{ S cm}^{-1}$, which is comparable to the pure IL conductivity of $5.28 \cdot 10^{-6} \text{ S cm}^{-1}$. Increasing or decreasing the IL loading from this ratio decreases the normalized conductivity. σ_{\perp} is lower than σ_{\parallel} for all the hPEMs; it significantly rises with electrolyte loading, and experiences a weak percolation-like behavior at 45 w/w% loading. As a result, the anisotropy increases to 5120 at 30 w/w% and then decreases to ~20 for 45 w/w% hPEM. Thicker films that were 70 μm thick were also tested to assure the characterizations are in the bulk property range, and not instead influenced by thin-film geometric effects. The conductivities of these thicker films were identical, within error, when compared to their 23 μm film counterparts.

As a baseline comparison, ionic conductivities of iPEMs were also measured. The normalized conductivity of the iPEMs did not significantly deviate from the range of loadings tested; however, the magnitude of the normalized conductivity was a factor of 20 lower than the pure IL, resolving more clearly the structural effects on ion conduction provided by HP.

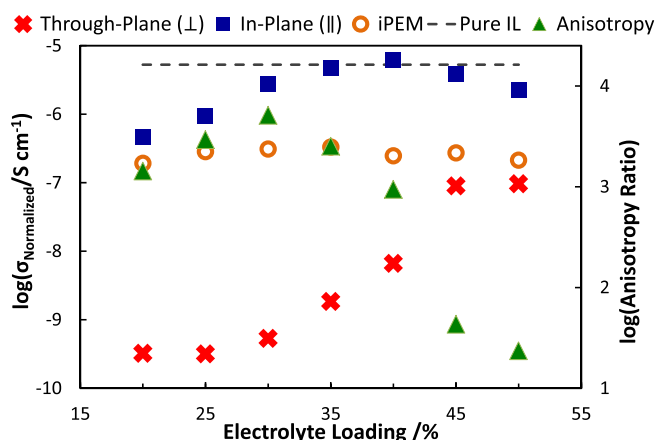


Fig. 4. Ionic conductivity measured via EIS normalized by IL volume fraction versus electrolyte content of hPEMs for \parallel (blue squares), \perp (red crosses) and isotropically polymerized membranes (orange circles) at room temperature. Anisotropic ratio of \parallel versus \perp is shown in green triangles. Error bars are on the same scale as the symbols. (For interpretation of the references to color in this figure legend, the reader is referred to the web version of this article.)

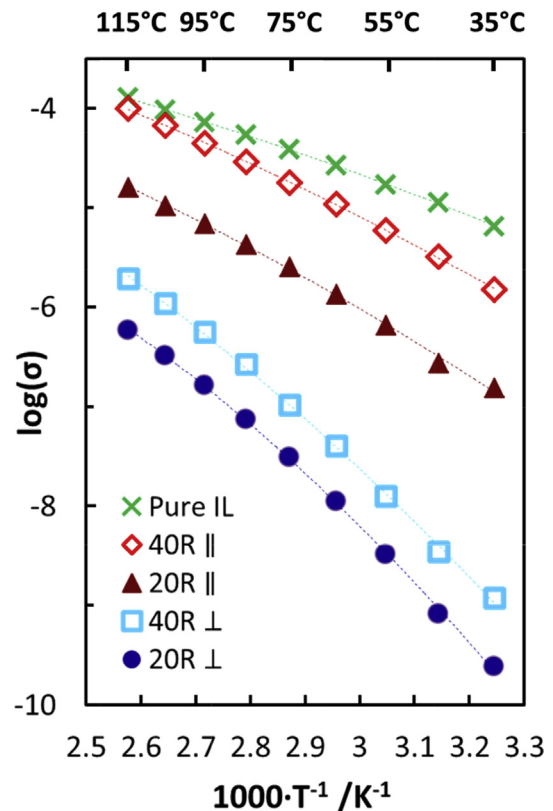


Fig. 5. EIS temperature scans showing temperature-dependent ionic conductivities of first heating for BrHTDP and second heating for 20 and 40 w/w% hPEMs.

4. Discussion

The above results show unprecedented directional control on ion transport in the hPEMs. To better understand the effect of interplay between phase separation and nanoconfinement effect on ion transport, the fabrication method must be examined. Many different factors influence the extent and localization of phase separation during the HP patterning process. The primary factors include the polymerization and diffusion kinetics of NOA65 reactive fluid and the miscibility between the IL and polymerizing NOA65. As the monomer concentration depletes in the constructive interference regions during the initial stage of polymerization, more monomer diffuses into the region to participate in the reaction. NOA65 polymerizes following a thiolene chemistry mechanism, which shows significantly slower network formation than comparable acrylate- or urethane-based photochemistries, and this shifts more control from the polymerization and diffusion kinetics over to thermodynamics with respect to polymer network and grating formation. As a result, more uniform, layered structures are formed in all IL-based hPEM samples. The relatively clean phase separation also results in the significant difference in ion conductivity between the in-plane and through-plane directions, with an extremely high conductivity anisotropy. The homogeneous NOA-rich layer “blocks” the through-plane ion transport. This control is governed by two factors; the concentration of ions in the NOA-rich layer, and the decrease of ion mobility caused by an increase in viscosity, which hinders ion flux. As the NOA65 monomer loading is decreased, the thickness of the NOA-rich layer decreases and the volume fraction of trapped ions increases. At a certain NOA-layer thickness and ion volume fraction, the ions are able to percolate through the depth of the NOA65 blockade. This percolation occurs

for one of two reasons: (1) at lower IL loadings, the grating formation dynamics are such that the trapped IL content is below the solubility limit after drying and aging the membranes, where the critical percolation concentration lies below the saturation limit; (2) at higher IL loadings, the IL content could surpass the solubility limit forming a sparse random nanochannel network via nanophase separation that cannot be observed under TEM. At lower electrolyte loadings, the NOA65 layer sufficiently arrests most ion flux; for all loadings, the \parallel conductivity was higher than \perp , with a maximum anisotropy of 5120 at 30% w/w%, showing these highly partitioned IL nanochannels give rise to unprecedented anisotropies.

To examine further the anisotropic behavior and partitioning effects, ionic conductivities were measured at elevated temperatures up to 115 °C in 10 °C increments, shown in Fig. 5. As the temperature is increased, the mobile IL molecules are expected to swell into the NOA65 matrix, which will give rise to a non-linear behavior. This subtle curvature can be seen between 35 °C and 115 °C; therefore, conductivity dependence on temperature does not follow an Arrhenius relationship. Instead, a Vogel–Tammann–Fulcher (VTF) fit results in R^2 values of >0.998 for all data sets. The VTF relation is expressed in Eq. (2):

$$\sigma = AT^{-\frac{1}{2}} \exp \left(\frac{-B}{T - T_0} \right), \quad (2)$$

where T_0 is the temperature at which the transport relationship ceases, which can be considered a temperature close to the glass transition temperature (T_g). [34,35] Since the pure IL also behaves with a VTF relationship to temperature, the ion flux must be affected by segmental motion of the long hydrocarbon chains in the cation, and the decrease in viscosity with temperature. Interestingly, T_0 is equal for the pure IL $40R_{\parallel}$ and $40R_{\perp}$ (175 K) suggesting that the IL and NOA65 were sufficiently partitioned so that the T_g of the IL-rich layers is not noticeably affected. Decreasing the electrolyte content to 20 w/w%, T_0 increases to 210–214 K, indicating that there is enough NOA65 content mixed in with the IL-rich layer region to increase the T_g of the system.

$40R_{\parallel}$ and $20R_{\parallel}$ slopes in Fig. 5 are similar to, but higher than, the pure electrolyte, evidence that the ion mobility for the \parallel direction is not significantly affected by the HP process. In this case, the limiting factor for ionic conductivity is the ion flux in the electrolyte-rich regions. The slopes of the \perp scans are approximately 2.5 times as large as the pure IL, which is in good agreement with the TEM investigations; since the ions must travel through the NOA65, the overall charge transport is limited by the ion flux in the polymer matrix, which is a function of the ion mobility activation energy and the concentration of ions in the NOA65. There are two factors that will decrease the membrane conductivity: (1) reducing the number of available ions available for mass transport, which is a function of system IL loading and IL dissociation in the electrolyte nanochannels; (2) increasing the activation energy will decrease the diffusivity of the charge carriers, and thus the ion flux, typically related to viscosity. The ionic conductivity, σ , can be correlated to the concentration of free ions, or ions contributing to charge flow, p , with the Nernst–Einstein relationship, Eq. (3):

$$\sigma = \frac{pq^2D}{k_B T}, \quad (3)$$

where diffusion can be described with the Arrhenius relationship shown in Eq. (4):

$$D = D_0 * e^{-\frac{E_A}{RT}}. \quad (4)$$

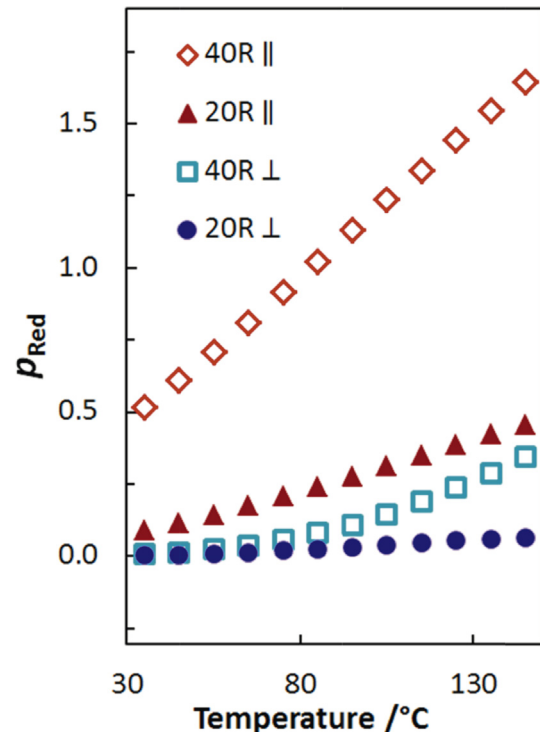


Fig. 6. Calculated p_{Red} versus temperature.

The reduced free ion charge carrier concentration of IL with respect to pure IL, $p_{\text{Red}} = p_{\text{grating}}/p_{\text{IL}}$, in the electrolyte-rich and NOA65 domains can be qualitatively calculated with respect to the pure IL using the slope and conductivity at a given temperature with Eq. (5):

$$\frac{\sigma_1}{\sigma_2} = \frac{p_1 * e^{-E_{A,1}}}{p_2 * e^{-E_{A,2}}}, \quad (5)$$

where q is constant, and D_0 is assumed to be constant, which is reasonable since the $\sigma_{\text{Normalized}}$ for all systems should converge to an intrinsic value as T approaches ∞ . Assuming that \parallel ion flux is provided by the IL-rich channels, and \perp ion flux is governed by the ion flux in the NOA65 as a system-limiting factor, then \parallel conductivity can be correlated reasonably with ions in the IL-rich phase, and \perp conductivity with ions captured in the NOA65-rich phase. At room temperature, $p_{\text{Red},\text{IL}} = 0.516$ and $p_{\text{Red},\text{NOA65}} = 0.007$ for $40R$, and for $20R$ $p_{\text{Red},\text{IL}} = 0.089$ and $p_{\text{Red},\text{NOA65}} = 0.003$, where by definition p_{Red} for pure IL is 1 at all T . This indicates that while the rigid NOA65 matrix reduces the mobility of the ions to cross across the NOA65 layers, in the NOA65-rich layers, a major factor to anisotropy contribution is ion volume exclusion, where the concentration of ions available for mass transport are reduced by factors of 35 and 75 for 20 and 40 w/w%, respectively. Using the VTF fitting curve, the slope at each point can be calculated, corresponding to the activation energy at the given temperature. Using this and combining it with the conductivity data, p_{Red} can be graphed versus temperature, shown in Fig. 6, extrapolated up to 150 °C using the VTF fitting. Interestingly, at lower temperatures the slopes of $40R_{\parallel}$ and $20R_{\parallel}$ are similar to the pure IL, meaning the activation energies should be similar, yet $20R_{\parallel}$ is offset by a factor of 40. The reduced ion concentration is low at lower temperatures, which resolves the discrepancy between the curves in Fig. 5. As temperature is increased, p for both $20R$ and $40R$ in both the NOA65-and IL-rich regions increases, suggesting ion aggregates decluster, increasing

the concentration of free ions. Particularly for $40R_{IL}$, p surpasses 1 at elevated temperatures, which suggests there is less ion clustering in the IL-rich electrolyte nanochannels than the pure IL. At this critical volume fraction loading of NOA65, the likely NOA65 dual-functionalizes as a scaffolding and an ion-dispersing agent, leading to an unaffected macroscopic ion flux. With proper material selection, this scaffolding dual-functionality phenomenon could be exploited to generate a new class of membrane materials with enhanced mechanical properties for electrochemical applications.

5. Conclusions

In summary, HP has been used to fabricate hPEMs to demonstrate a decoupling of ion transport with mechanical enhancement, converting a liquid electrolyte to a free-standing membrane. The morphology and conductivity of these films have been systematically studied using UV–Vis, TEM and EIS techniques. When the thermodynamics and kinetics of the HP components are properly balanced, a conductivity anisotropy over 5000 has been achieved, with minimal effects on in-plane ion flux in the membrane. This HP technique can be translated into various periodic geometries, via a large variety of prepolymer choices. Our results show that with proper material selection, hPEMs will be viable candidates for next generation electrochemical membranes, and will serve as a platform for understanding the interdependency of nano-confinement and ion flux.

Acknowledgments

CYL is grateful for the support from the National Science Foundation through grants CMMI-1334067. DMS would like to acknowledge the NSF IGERT and GRFP fellowship support.

References

- [1] G.M. Stone, S.A. Mullin, A.A. Teran, D.T. Hallinan, A.M. Minor, A. Hexemer, N.P. Balsara, *J. Electrochem. Soc.* 159 (2012) A222–A227.
- [2] S. Vorrey, D. Teeters, *Electrochim. Acta* 48 (2003) 2137–2141.
- [3] E.A. Jackson, M.A. Hillmyer, *ACS Nano* 4 (2010) 3548–3553.
- [4] M. Ulbricht, O. Schuster, W. Ansorge, M. Ruetering, P. Steiger, *Sep. Purif. Technol.* 57 (2007) 63–73.
- [5] A.G. Mayes, J. Blyth, M. Kyrolainen-Reay, R.B. Millington, C.R. Lowe, *Anal. Chem.* 71 (1999) 3390–3396.
- [6] S.H. Kim, K. Hong, W. Xie, K.H. Lee, S. Zhang, T.P. Lodge, C.D. Frisbie, *Adv. Mater.* 25 (2013) 1822–1846.
- [7] K.M. Cable, K.A. Mauritz, R.B. Moore, *Chem. Mater.* 7 (1995) 1601–1603.
- [8] R. Mäki-Ontto, K. de Moel, E. Polushkin, G. Alberda van Ekenstein, G. ten Brinke, O. Ikkala, *Adv. Mater.* 14 (2002) 357.
- [9] M. Yoshio, T. Kagata, K. Hoshino, T. Mukai, H. Ohno, T. Kato, *J. Am. Chem. Soc.* 128 (2006) 5570–5577.
- [10] M.J. Park, N.P. Balsara, *Macromolecules* 43 (2010) 292–298.
- [11] P.W. Majewski, M. Gopinadhan, W.S. Jang, J.L. Lutkenhaus, C.O. Osuji, *J. Am. Chem. Soc.* 132 (2010) 17516–17522.
- [12] P.W. Majewski, C.O. Osuji, *Langmuir* 26 (2010) 8737–8742.
- [13] Y.A. Elabd, C.W. Walker, F.L. Beyer, *J. Membr. Sci.* 231 (2004) 181–188.
- [14] H. Hu, S. Rangou, M. Kim, P. Gopalan, V. Filiz, A. Avgeropoulos, C.O. Osuji, *ACS Nano* 7 (2013) 2960–2970.
- [15] K. Kishimoto, M. Yoshio, T. Mukai, M. Yoshizawa, H. Ohno, T. Kato, *J. Am. Chem. Soc.* 125 (2003) 3196–3197.
- [16] L. Ramón-Giménez, R. Storz, J. Haberl, H. Finkelmann, A. Hoffmann, *Macromol. Rapid Commun.* 33 (2012) 386–391.
- [17] A. Abate, A. Petrozza, G. Cavallo, G. Lanzani, F. Matteucci, D.W. Bruce, N. Houbenov, P. Metrangolo, G. Resnati, *J. Mater. Chem. A* 1 (2013) 6572–6578.
- [18] D. Golodnitsky, E. Peled, *Electrochim. Acta* 45 (2000) 1431–1436.
- [19] N.S. Wanakule, A. Panday, S.A. Mullin, E. Gann, A. Hexemer, N.P. Balsara, *Macromolecules* 42 (2009) 5642–5651.
- [20] G. Sudre, S. Inceoglu, P. Cotanda, N.P. Balsara, *Macromolecules* 46 (2013) 1519–1527.
- [21] Y.A. Elabd, M.A. Hickner, *Macromolecules* 44 (2011) 1–11.
- [22] T.J. Bunning, L.V. Natarajan, V.P. Tondiglia, R.L. Sutherland, *Annu. Rev. Mater. Sci.* 30 (2000) 83–115.
- [23] L.V. Natarajan, C.K. Shepherd, D.M. Brandelik, R.L. Sutherland, S. Chandra, V.P. Tondiglia, D. Tomlin, T.J. Bunning, *Chem. Mater.* 15 (2003) 2477–2484.
- [24] R.A. Vaia, C.L. Dennis, L.V. Natarajan, V.P. Tondiglia, D.W. Tomlin, T.J. Bunning, *Adv. Mater.* 13 (2001) 1570–1574.
- [25] J.D. Busbee, A.T. yuhl, L.V. Natarajan, V.P. Tongdilia, T.J. Bunning, R.A. Vaia, P.V. Braun, *Adv. Mater.* 21 (2009) 3659–3662.
- [26] N. Suzuki, Y. Tomita, T. Kojima, *Appl. Phys. Lett.* 81 (2002) 4121–4123.
- [27] T.N. Smirnova, O.V. Sakhno, P.V. Yezhov, L.M. Kokhtych, L.M. Goldenberg, J. Stumpe, *Nanotechnology* 20 (2009) 245707.
- [28] C.Y. Li, M.J. Birnkrant, L.V. Natarajan, V.P. Tondiglia, P.F. Lloyd, R.L. Sutherland, T.J. Bunning, *Soft Matter* 1 (2005) 238–242.
- [29] M.J. Birnkrant, H.K. McWilliams, C.Y. Li, L.V. Natarajan, V.P. Tondiglia, R.L. Sutherland, P.F. Lloyd, T.J. Bunning, *Polymer* 47 (2006) 8147–8154.
- [30] M.J. Birnkrant, C.Y. Li, L.V. Natarajan, V.P. Tondiglia, R.L. Sutherland, P.F. Lloyd, T.J. Bunning, *Nano Lett.* 7 (2007) 3128–3133.
- [31] M.J. Birnkrant, C.Y. Li, L.V. Natarajan, V.P. Tondiglia, R.L. Sutherland, T.J. Bunning, *Soft Matter* 7 (2011) 4729–4734.
- [32] D.M. Smith, B. Dong, R.W. Marron, M.J. Birnkrant, Y.A. Elabd, L.V. Natarajan, V.P. Tondiglia, T.J. Bunning, C.Y. Li, *Nano Lett.* 12 (2012) 310–314.
- [33] T. Welton, *Chem. Rev.* 99 (1999) 2071–2084.
- [34] T. Fujinami, Y. Buzoujima, *J. Power Sources* 119 (2003) 438–441.
- [35] B. Papke, M. Ratner, D. Shriver, *J. Electrochem. Soc.* 129 (1982) 1694–1701.